International Journal of Impact Engineering 182 (2023) 104783

Contents lists available at ScienceDirect

International Journal of Impact Engineering

journal homepage: www.elsevier.com/locate/ijimpeng

Improved analysis for impact response prediction of reinforced concrete structures considering stress wave propagation and time dependent shape function

Liuliang Cui [a], Xihong Zhang [a,*], Hong Hao [b]

[a] Centre for Infrastructure Monitoring and Protection, School of Civil and Mechanical Engineering, Curtin University, Kent Street, Bentley, Australia
[b] Earthquake Engineering Research and Test Center, Guangzhou University, China and Centre for Infrastructure Monitoring and Protection, School of Civil and Mechanical Engineering, Curtin University, Kent Street, Bentley, Australia

ARTICLE INFO

Keywords:
Reinforced concrete
SDOF
Impact loading
Wave propagation effect
Time-dependent shape function
Analytical methods

ABSTRACT

In the design of reinforced concrete (RC) structures subjected to impulsive loading, usually an equivalent Single-Degree-of-Freedom (SDOF) system is derived based on a constant deflection shape assumption corresponding to static-loading condition. It is commonly known that this idealized assumption may not necessarily lead to accurate predictions of structural responses. This paper presents an improved analytical approach to predict the dynamic response of RC beams with consideration of stress wave propagation effect in the beam in the initial stage upon impact load application, and time-dependent shape function for SDOF analysis. The response of a structural component is divided into two phases: local response phase which is calculated using governing equations of stress wave propagations; and global response phase analyzed using the equivalent SDOF systems with considerations of time-dependent deformation shapes. Laboratory drop-weight impact tests are performed on RC beams, which are used to validate the developed method. Further validation is carried out against existing testing results by other researchers, demonstrating the proposed approach offers more accurate predictions of RC beam responses under impact loading compared to the conventional SDOF method.

1. Introduction

The behavior of reinforced concrete (RC) structures under impulsive loading, such as blast and impact loads, needs to be considered for structural safety in designing critical civil structures. Numerous laboratory and field testing, as well as post-event investigations showed the responses of RC structures under impulsive loading differ significantly from their static responses. This is because under impulsive loading, intensive energy released in a brief period leads to various phenomena affecting both the material behavior (e.g., dynamic increase effect on material strength) and structural response (e.g., stress wave propagation in structure and excitation of higher response modes), resulting in spalling and crushing damages and shear governed failure in lieu of flexural deformation. When subjected to impulsive loading, materials experiencing high strain rates exhibit increased strength and modulus, and reduced ductility [1,2], while wave propagation effects and inertia effects concurrently exert a significant influence on the structural response [3–5]. Therefore, it is essential to accurately analyze the response of structures under dynamic loading for effective and efficient engineering design.

Previous studies revealed a noticeable delay between the instance of impact loading acting on a RC beam and the activation of the support reactions [6,7]. This delay signifies that the impact load is balanced primarily by inertial resistance, and the initial deformation shape of the beam will be changing over time as not the entire beam is activated to resist the impact load. This leads to remarkably different response characteristics of the beam from that when it is subjected to a static load. Given that it takes time for the effect of load to spread over the entire structure, certain parts of the beam initially do not contribute to resisting the applied dynamic load as evidenced by zero initial reaction force. This phase of response is referred to as the local response phase [8,9], in which a growing number of sections of the beam are gradually activated to resist the applied load, as a result, the deformation shape of the beam changes as the stress wave propagates. For analysis, it typically assumes that a plastic hinge is formed at the impact location with the affected portion of the beam responding as though it was a fixed beam

* Corresponding author.
E-mail address: xihong.zhang@curtin.edu.au (X. Zhang).

https://doi.org/10.1016/j.ijimpeng.2023.104783
Received 6 August 2023; Received in revised form 12 September 2023; Accepted 15 September 2023
Available online 16 September 2023

with an effective span length (L_{eff}) shorter than the actual beam span [9–11]. The effective span length expands over time as stress wave propagates during the local response phase. The time required for the wave to reach the supports is dependent on the beam length and the average force propagation velocity. Once the whole beam is activated, the deformation shape of the beam could be approximated to that under static loading [10]. Since the above-described beam behavior takes time to accomplish, the deformation shape of the beam during this period is a time-dependent function, whose influence on the overall dynamic response of the beam remains not fully assessed as the current analysis and design normally adopt a constant deflection shape of the beam under static loading in the derivation of equivalent SDOF system.

Hard impacts or sudden and forceful collisions typically result in the generation of multiple types of waves emanating from the impact point [12]. The longitudinal wave, traveling the fastest, propagates in the loading direction, which is followed by the shear wave that travels in the direction perpendicular to the impact direction. The longitudinal wave has an approximate speed of 3300 m/s, while the shear wave travels at a velocity of around 2300 m/s in concrete [12]. Furthermore, the flexural wave propagates as a physical disturbance, also moving transversely in the impact direction [10]. It is posited that the local response of a structure is primarily induced by the flexural wave. Jones [10] assumed a linear transvers velocity profile for the flexural wave, and proposed a formula to determine the wave propagation velocity, where beam density, beam length, impactor mass, impact velocity and the sectional moment resistance capacity are considered. Some researchers discovered that the velocity of the flexural wave can be considerably lower than that of the shear wave [13], which also decreases roughly in proportion to the increase of beam slenderness (approximately 250–1000 m/s for length-to-depth ratios of the beam ranging between 10 and 4) [6]. Overall, to accurately analyze the local response of the RC beam, it is necessary to properly evaluate stress wave propagation within the structure.

Nonlinear finite-element models are frequently employed to investigate the behavior of RC structures under impact loading because they can easily characterize those intricate phenomena, including concrete cracking and crushing, reinforcement yielding, and debonding between reinforcement and concrete [14,15]. Simplified computational tools, derived from spring-mass models with single degree of freedom (SDOF) or multiple degrees of freedom (MDOF) systems, are extensively utilized in the practical design of impulse-loaded structures [8,9,16-19]. Such tools are advantageous in the sense that they provide an improved understanding about the fundamental physics behind complex events. Moreover, their rapid execution enables a powerful analysis, as numerous calculations can be swiftly performed once defined. The improvement of such simplified methods is also the focus of various studies. For instance, Cui et al. [18] considered strain hardening and softening behaviors of a structural component, and generated design charts following UFC-3–340–02 for SDOF analysis with improved accuracy. Compressive and tensile membrane effects that are commonly observed in RC beams have also been accounted for in the determination of resistance functions for more accurate prediction of structural responses using conventional SDOF analysis method [19,20]. To assess the influence of shear failure mode, Wei et al. [9] and Zhao et al. [21] introduced a dynamic failure criterion based on the Modified Compression Field Theory (MCFT) into the MDOF systems to predict shear resistance and the occurrence of shear failure.

Nevertheless, most simplified models do not account for wave propagation effect and structure deformation shape variations that significantly influence the effective mass, loading capacity, and overall response of a structural element. Owing to stress wave propagation effect, the distribution of dynamic moments and shear forces along the beam may remarkedly differ from that under static loading condition. Some researchers incorporated the wave propagation effect into the Two-Degree-of-Freedom system (TDOF) to predict the impact responses [9,22]. In the calculation of local response, the equations of motion are the same as conventional TDOF method except that the beam length is replaced by the effective length (L_{eff}). However, the effective length is calculated based on shear wave velocity (2300 m/s in concrete) which is much larger than the observed wave velocities (250–1000 m/s) [6]. During the local response phase, the supports are not yet to contribute to resisting the force applied by the impact. Instead, inertia resistance of the beam acts to resist the impact force to attain dynamic equilibrium [10,13]. In the global response phase, despite the variation of the deformation shape, the effective length of the beam remains constant, allowing for the development of simplified analytical models, such as SDOF models, with time-dependent mass factors to characterize the response behavior.

This study introduces an improved analytical method to predict the complete impact response behavior of RC beams, where both wave propagation effect during the local response phase and time-dependent deformation shape during the global response phase are considered. Laboratory impact tests are carried out to investigate the dynamic response of RC beams. Utilizing digital image correlation (DIC) techniques, wave propagation phenomena are observed, and time-dependent deformation profiles of the beam during the impact process are quantified. The laboratory testing data are then used to verify the accuracy of the developed analytical models. Existing testing data by other researchers are also used for further verification of the proposed methods.

2. Experimental investigation

2.1. Test details

Laboratory impact tests are designed and performed to investigate the dynamic behavior of RC beams under impact loading. Three identical RC beams, as depicted in Fig. 1, are designed and fabricated in accordance with AS 3600 [23]. The beams are 2000 mm long with a cross-section of 150 mm × 150 mm. The longitudinal reinforcements are composed of four N12 rebars with 20 mm thick concrete cover. This configuration corresponds to a tension reinforcement ratio of $\rho = 1.32\%$ ($\rho = A_s/bd$, where A_s represents the area of tensile reinforcement, b denotes the width of beam cross-section, d refers to the distance between the extreme compression fiber and the centroid of tension reinforcement). The longitudinal reinforcements extend continuously from the beam into two robustly reinforced concrete footings of 750 mm in height, 500 mm in length, and 300 mm in width. These reinforcements are bent which protrude through the top face of the footing, being subsequently anchored using steel plates to ensure adequate anchorage. A strong anchorage is thus achieved for the beams. The transverse reinforcements, with a diameter of 10 mm, are uniformly distributed along the beam length at 200 mm intervals.

Table 1 lists the material properties of all reinforcements, as provided by the suppliers. Both types of rebars possess a yielding strength of 500 MPa and an elastic modulus of 200 GPa. C40 concrete is used for beam cast, which undergoes ambient curing. Standard compressive tests on concrete cylinders reveal the average compressive strength and elastic modulus of 41.37 MPa and 27.98 GPa, respectively.

Two replicated specimens (designated as DM1T1 and DM2T1) are prepared to be fully restrained in all directions to replicate the boundary conditions of RC beams with strong column and/or wall restraints, which thereby significantly induce membrane actions. Conversely, a third specimen (labeled as DC1T1) is only restrained against the rotational and vertical movements, while its lateral restraints are released. It thus precludes the presence of membrane actions. To ensure sufficient restraint for beams DM1T1 and DM2T1, particularly in the longitudinal direction, a specialized reaction frame is designed and fabricated, and four 20 mm diameter Reidbars (yield strength 500 MPa, and Young's modulus 200 GPa) are utilized to connect the reaction frames along the longitudinal direction of the beam, as depicted in Fig. 2(a) and (c). A comprehensive description of the reaction frame can be found in

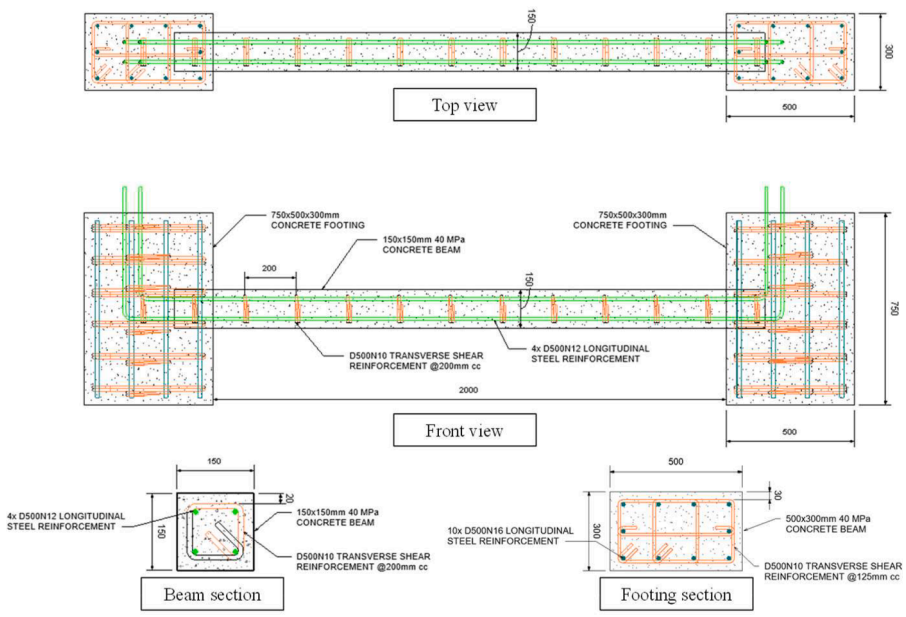

Fig. 1. Geometry and reinforcement arrangement of concrete beam specimens (unit: mm).

Table 1
Material properties of reinforcements.

Material	Diameter (mm)	Yield strength (MPa)	Elastic modulus (GPa)
N10	10	500	200
N12	12	500	200
N16	16	500	200

Ref. [19] which focuses on analyzing the membrane effects. For beam DC1T1, the longitudinal restraint at the right end of the beam is released by removing the end support and disconnecting the Reidbars between the two footings, as illustrated in Fig. 2(b).

During the testing, a 200 kg drop weight is released from a height of 3.2 m to impact at the midspan of the beams. To ensure the impactor descends vertically toward the targets, a PVC guiding tube is utilized and affixed to a steel frame. A load cell, secured at the center-top surface of the beams, records the impact force at a frequency of 96 kHz. Additionally, a 15 mm thick rubber is attached to the top surface of the load cell to more uniformly distribute the impact force onto the impact area of the RC beam. A high-speed camera with 8000 fps is employed to record the deformation-to-failure process of each beam. Owing to space constraints and symmetric response assumption, only a half of the beam

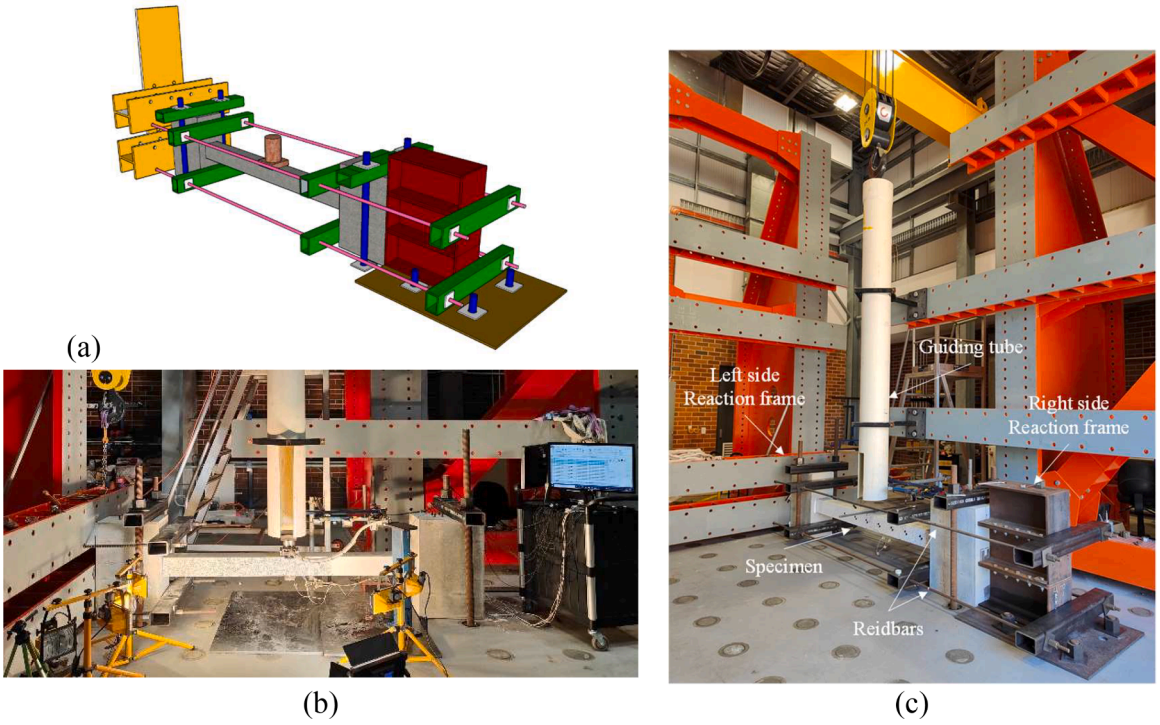

Fig. 2. (a) Schematic view of the test setup for restrained specimens; (b) test setup of unrestrained specimen DC1T1 and (c) test setup of restrained specimens DM1T1 and DM2T1.

is monitored. The captured images are analyzed using Digital Image Correlation (DIC) software, which measures the changing deflected profiles in subsequent images.

2.2. Test results

2.2.1. Beam damage and response

Fig. 3 presents photographs of the tested beams after the impact tests. As observed, flexural cracks are visible at the midspan of the beams. Additionally, all beams exhibit extensive diagonal shear cracks at the supports and concrete crushing on the bottom face at the supports. The development of shear cracks on only one side of the beams, i.e., unsymmetrical damage, may be attributed to unavoidable manufacturing inconsistencies or some initial defects (e.g., voids in concrete). Once the shear failure occurred at one side of the beam, the impact energy would be dissipated mainly by the damaged area. Thus, it would be hard for the other side to form another large shear crack.

Fig. 4(a) illustrates the measured impact force time histories for the three tested beams DM1T1, DM2T1 and DC1T1. The measured impact loads are characterized with an initial pulse of relatively high amplitudes, succeeded by a blunt waveform with comparatively low amplitudes. The amplitude of the peak and the duration of the initial pulse in these three beams are nearly identical because the initial impact force is governed primarily by the impact velocity and contact stiffness [24]. The peak impact force for specimen DC1T1 reaches approximately 220 kN at around 2 ms, with the total duration of the impact load lasting about 60 ms. However, the subsequent plateau of DC1T1 slightly differs from those of DM1T1 and DM2T1, which is mainly due to the variations of beams global stiffness [24].

Fig. 4(b) displays the midspan deflection time histories of the three beams, which are obtained from the DIC analysis. Table 2 summarizes the impact testing results. As expected, beam DC1T1 exhibits the highest peak deflection (93.7 mm) among the three beams, since its lateral movement is unrestrained at its ends. The maximum deflections of DM1T1 and DM2T1 are 79.2 mm and 86.3 mm, respectively. The difference can be attributed to the inevitable difference in fabrications. The difference between DM2T1 and DC1T1 is 8.6%. As noted by Cui [20], despite the absence of a lateral restrain to DC1T1, rotational and vertical restraints would induce substantial constraint to support movement. Friction between the footing and the floor also introduces additional lateral restraint to DC1T1. As a result, the deflection of DC1T1 is not significantly different from that of DM1T1.

2.2.2. Deformation-to-failure process

To investigate the dynamic response of RC beams under impact load, the deformation-to-failure processes of the beams are analyzed using DIC technique. Fig. 5 shows the major strain contours of the fully restrained beam DM1T1 from high-speed camera images, which offers a convenient method for observing strain distributions and failure patterns. At $t = 2$ ms, the impact force reaches its maximum, but the mid-span deflection is only 4.7 mm. Deformation is primarily concentrated at the midspan, and no crack appears at this instant. At $t = 5.3$ ms, the impact force quickly decreases to a much smaller amplitude, and the mid-span deflection increases to 20.8 mm. At this point, flexural cracks are developed at the bottom face of the midspan and the top face of the beam near the supports. At around $t = 11.1$ ms, a diagonal shear crack is observed near the support, flexural cracks at mid-span are widened, and concrete begins to crush at the compression zone. When the mid-span deflection reaches its maximum of 79.2 mm, more severe concrete damages can be observed at the support and the mid-span of the beam. The diagonal shear crack penetrates through the whole depth of the beam, accompanied by severe concrete crushing and spalling.

Fig. 6 displays the major strain contours of DC1T1 during the deformation-to-failure process. Similar to DM1T1, high tensile strains can be found on the bottom face of the beam at mid-span, vertical cracks are initiated at both midspan and near the support due to excessive flexural bending deformation. Unlike DM1T1, the primary diagonal shear crack of DC1T1 occurs on the right side of the beam support. As can be seen in Fig. 3(a), no obvious shear crack is observed on the left side of the beam, which is different to specimen DM1T1. The strain contours of DM1T1 and DC1T1 depict a complete damage-to-failure process of the beams subjected to impact load.

2.2.3. Deformation shapes and load-mass factors

The deflection time histories of each beam during the testing process are processed to derive the time-dependent deflection profile of the beam. Fig. 7 shows the deflection profiles of beam DM1T1 (half beam) during the first few milliseconds of its response upon the impact. The profiles are plotted by extracting the deflections of points along the central line of the beam shown as the black line in Figs. 5 and 6. As

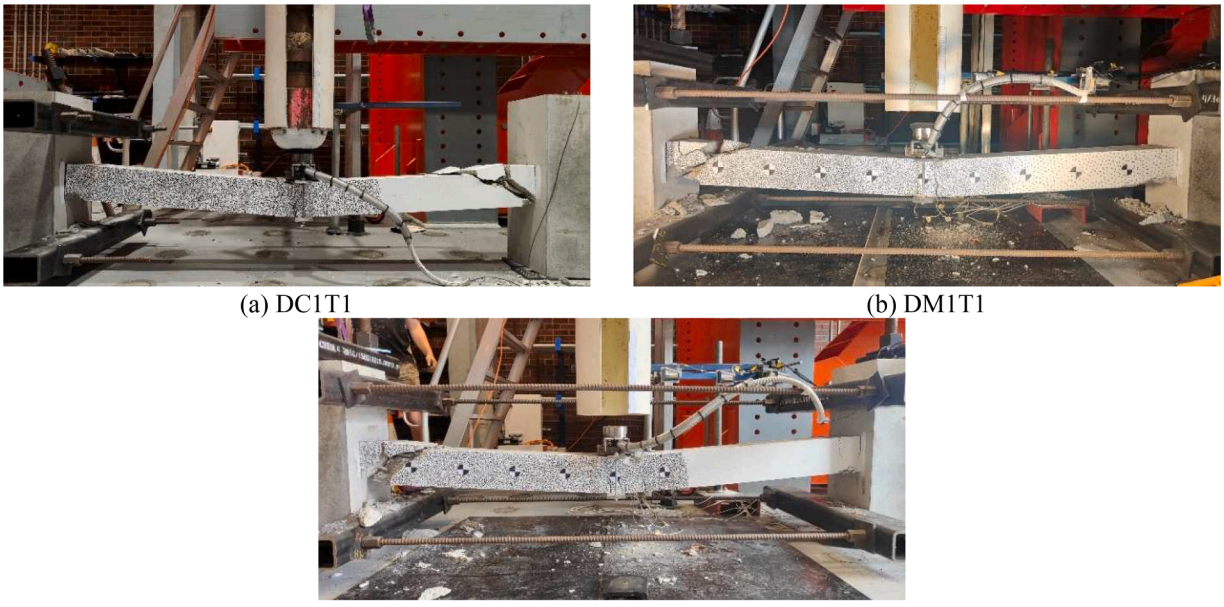

Fig. 3. Images of the post-test beams, (a) DC1T1, (b) DM1T1 and (c) DM2T1.

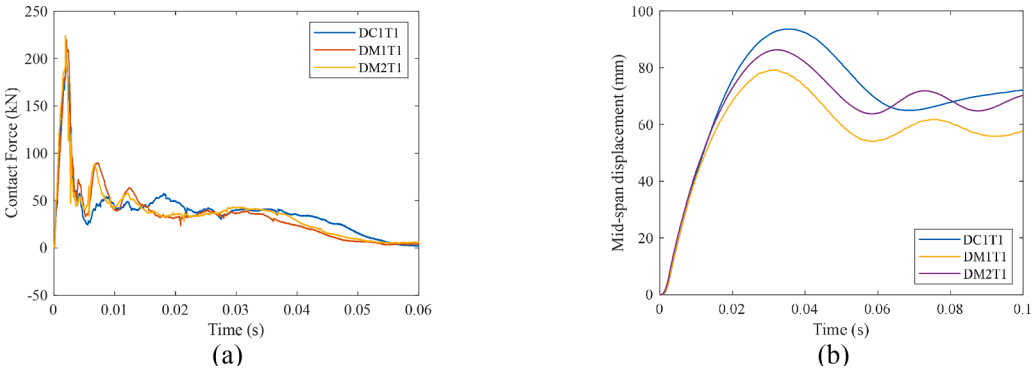

Fig. 4. (a) Time-histories of impact forces; (b) Load-deflection curves at midspan of different specimens.

Table 2
Summary of impact test results.

Specimen No.	Peak impact load (kN)	Time at peak impact load (ms)	Maximum mid-span deflection (mm)	Time taken to achieve the maximum deflection (ms)
DC1	216.1	2.00	93.7	35.5
DM1	220.0	1.92	79.2	31.3
DM2	224.2	2.08	86.3	32.4

shown in Fig. 7, it is evident that only a small section of the beam is deforming transversely to the impact direction in the early stage. It verifies that not the entire beam is excited and thus responds to the impact force at the instance of impact. As the flexural wave travels towards the support, a larger section of the beam is excited and begins to respond to the impact. This causes the effective length of the beam to increase with time. Prior to the flexural wave reaching the support, no reaction from the supports contributes to resisting the impact force. Thus, the impact force is resisted primarily by inertial force. During this period, the deflection profiles exhibit a typical elastic deformed shape expected for a fixed beam. From deflection profiles shown in Fig. 7(a), it can be estimated that the wave propagation time (the time from the occurrence of impact to the wave reaching the support) is approximately 2 ms, which is very close to the time when the recorded impact load reaches the first peak in the force time history. This propagation time corresponds to an average wave propagation velocity of 500 m/s.

Fig. 7(b) exhibits the normalized deformation shape of beam DM1 at different time instants. It is obvious that the deformation shape keeps changing especially during the initial 2 ms upon impact. After the entire beam is excited at $t = 5.25$ ms, the normalized deformation shape of beam DM1 remains almost unchanged. Therefore, to properly analyse the dynamic response of a RC beam subjected to impact loading, it is necessary to account for wave propagation effect and time-dependent deformation shape function.

Based on the deflection shape obtained from the above DIC analysis, the mass-factor-deflection characteristics of the three tested beam specimens are generated and plotted in Fig. 8.

The mass factor K_M for a distributed mass of beam can be calculated as

$$K_M = \frac{2\int_0^L m\phi^2(x,t)dx}{M_b} \tag{1a}$$

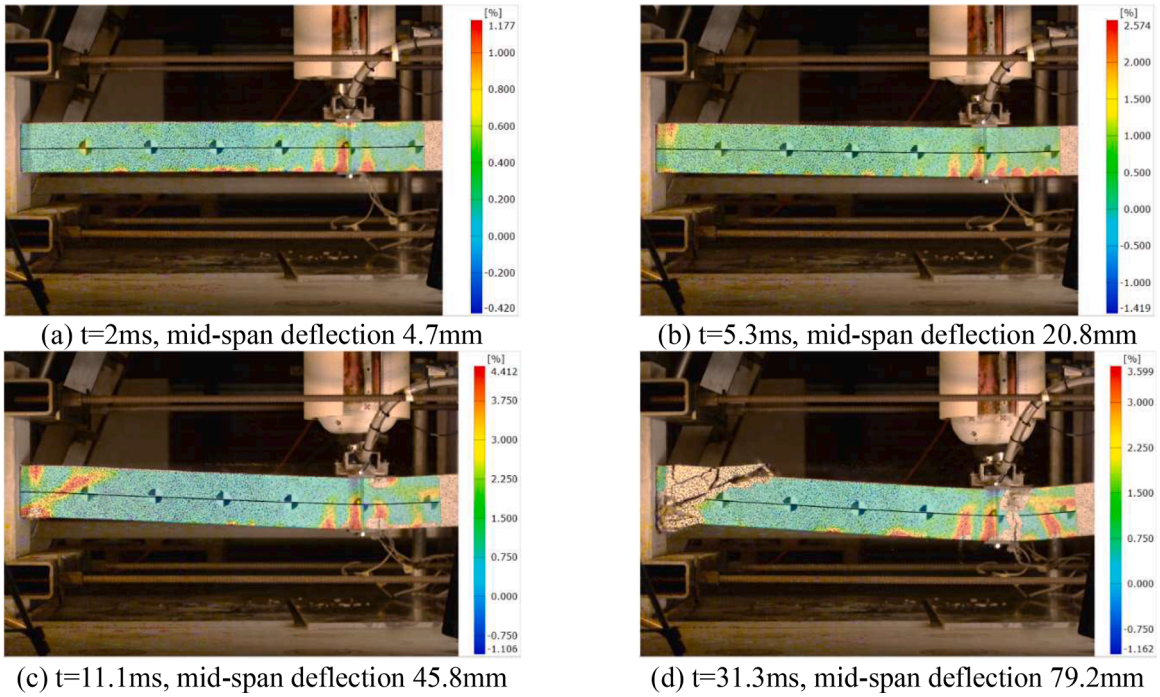

Fig. 5. Major strain contours of beam DM1T1 during the deformation-to-failure process.

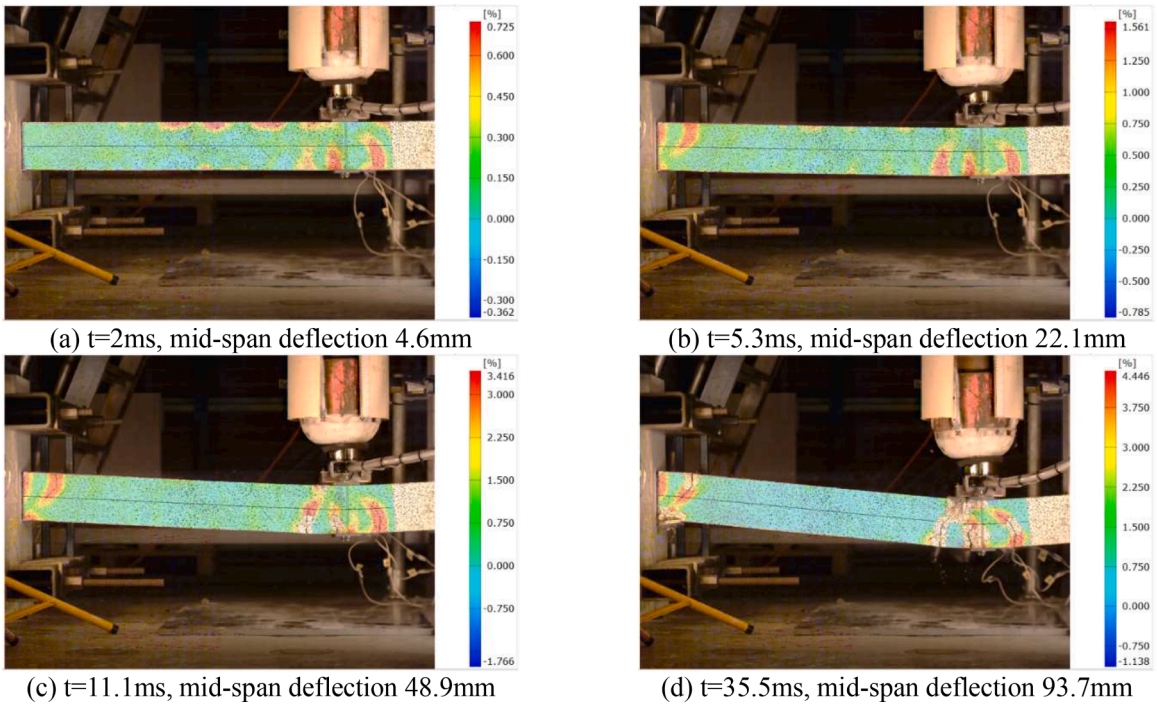

Fig. 6. Major strain contours of beam DC1T1 during the deformation-to-failure process.

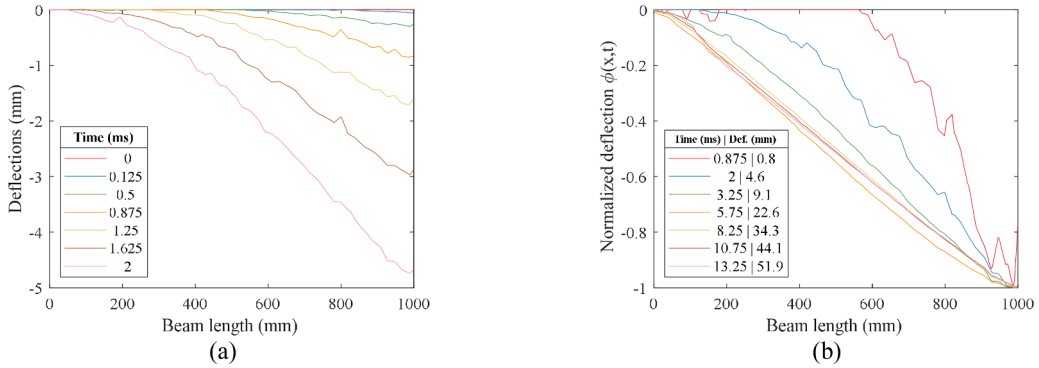

Fig. 7. (a) Deformation profiles of beam DM1 during 0–2 ms; (b) Normalized deformation shape of beam DM1 at different time instants and deflections.

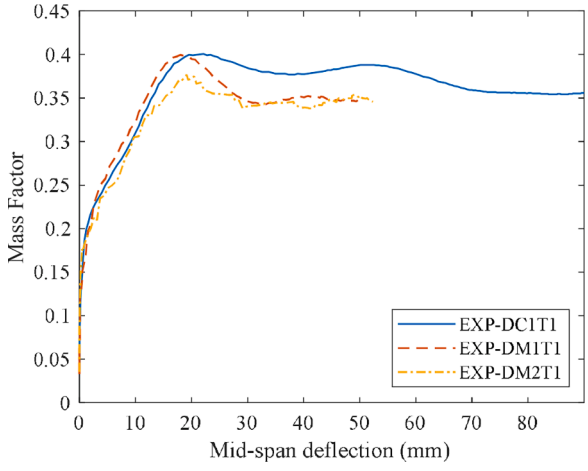

Fig. 8. Mass factor K_m vs mid-span deflection obtained from DIC analysis.

and for a concentrated mass system,

$$K_M = \frac{\sum_{r=1}^{i} M_r \phi_r^2}{M_b} \tag{1b}$$

where m is the mass per unit length; $\phi(x,t)$ is the shape function, $\phi(x,t) = u(x,t)/u_m$, with $u(x,t)$ denoting the deflection profile and u_m signifying the maximum deflection; $\phi_r = u_r/u_m$, where u_r is the deflection at mass r; M_b is the total mass of the beam.

From observations in Fig. 7(a) and Fig. 8, at $t = 2$ ms the flexural wave just reaches the support, the equivalent mass factor quickly rises to around 0.23 almost instantaneously with a very small beam midspan deflection (only 4.6 mm). The equivalent mass factor increases almost linearly with the deflection. Afterwards, the equivalent mass factor begins to increase at a smaller rate when the entire beam is excited and participates to the dynamic response. Once the mid-span deflection reaches around 20 mm, flexural cracks emerge at the midspan and supports, and the equivalent mass factor attains its maximum ranging between 0.38 and 0.4. Prior to this, the mass-factor versus midspan-deflection curves of all three specimens are very close to each other. As the plastic deformation and cracks grow, the equivalent mass factor begins to decrease. For specimens DM1T1 and DM2T1, their mass

factors decrease rapidly after their midspan deflection reaching 20 mm to approximately 0.345, then fluctuate for a period until the diagonal shear crack penetrates through the whole depth of the beam when the midspan deflection reaches 52 mm. For specimen DC1T1, the mass factor decreases slowly eventually approaching 0.345 when the entire beam collapses. The different mass factors between DM1T1 and DC1T1 could be attributed to the different boundary conditions.

Overall, from the above laboratory impact test, it could be found that to properly analyse the dynamic response of a RC beam subjected to impact loading, it is necessary to account for wave propagation effect considering the effective beam length that participates in dynamic response of the RC beam when subjected to impact loading. Also, it is important to consider the time-dependent deformation shape of the RC beam, which results in varying equivalent mass factors and thus dynamic beam response under impact loading.

3. Proposed analytical method for predicting impact responses

This section introduces an improved analytical method to predict the dynamic responses, which considers both wave propagation effects and time-dependent deformation shape of the structure in deriving the equivalent SDOF system. Taking a fully clamped RC beam as an example without losing generality, as shown in Fig. 9(a), the beam with a length of 2 L is struck at the mid-span by a mass M traveling with an initial velocity V_0. Assuming the impactor remains in contact with the beam after the impact and travels with the beam at mid-span with the same velocity V_0 and the rest of the beam is at stationary state, to maintain dynamic equilibrium, stress waves are generated which propagate away from the mid-span towards the two supports.

In fact, two distinct phases of motion will occur [10]: in the first phase of motion, a flexural wave is developed under the impact location at $t = 0$, and two travelling hinges propagate from the mid-span towards the supports, traveling through the undeformed sections of the beam. The effective length λ increases with the propagation of the traveling hinges, as shown in Fig. 9(b). At $t = t_1$, the flexural wave reaches the supports, but the transvers velocity is not zero. Therefore, the beam will continue to move transversely until the beam come to rest, which is the second phase of motion. In this phase, support reactions play an important role in resisting the impact load, while stress wave effect diminishes and has negligible influences. The response of the beam is then governed by the global dynamic response modes which could be approximately represented by using an equivalent SDOF system.

3.1. Local response phase (wave propagation phase)

As described above, in the first phase of motion, a flexural wave is generated which propagates from the impact point along the beam to the supports. This process can be expressed following Jones' analytical solution [10]. Being different from Jones's method which assumes a linear transvers velocity profile, in this study the transverse velocity profile of the beam is assumed the same as the static shape of a fixed beam subjected to a concentrated loading. The velocity profile for the right half of the beam can be written as

$$\dot{u}(x) = \dot{U}\left(\frac{2x^3}{\lambda^3} - \frac{3x^2}{\lambda^2} + 1\right),\ 0 \le x \le \lambda \tag{2a}$$

and

$$\dot{u}(x) = 0,\ \lambda \le x \le L/2 \tag{2b}$$

where λ is the effective length of the beam, which is the time-dependent location of the travelling hinge; $\dot{u}(x)$ is the transvers velocity of the beam; and $\dot{U}$ is the transvers velocity of the beam at mid-span.

Considering the vertical momentum equilibrium for the central portion of the beam between the two travelling hinges, it has

$$MV_0 = M\dot{U} + 2\int_0^{\lambda} m\dot{u}(x)dx \tag{3}$$

where m is the mass per unit length of the beam, M is the mass of the impactor, and V_0 is the impact velocity. Substituting Eq. (2a) into (3), it gives

$$MV_0 = M\dot{U} + 2\int_0^{\lambda} m\dot{U}\left(\frac{2x^3}{\lambda^3} - \frac{3x^2}{\lambda^2} + 1\right)dx \tag{4}$$

or

$$MV_0 = M\dot{U} + \lambda m\dot{U} \tag{5}$$

Therefore

$$\dot{U} = V_0 \Big/ \left(1 + \frac{m\lambda}{M}\right) \tag{6}$$

Now considering the bending moment equilibrium of the portion $0 \le x \le \lambda$ with travelling hinges at $x = 0$ and $x = \lambda$, for simplification, it is assumed that the moments at the travelling hinges and the mid-span remain constant equalling to the section yielding moment M_0 during the wave propagation phase. This assumption has been verified to yield good predictions by previous researchers [10]. Thus, taking moments equilibrium about the mid-span gives

$$2M_0 - \int_0^{\lambda} m\ddot{u}(x)xdx = 0 \tag{7}$$

since the shear force $Q = 0$ at $x = \lambda$. Substituting Eq. (2a) into (7), it yields

$$\int_0^{\lambda} m\left[\ddot{U}\left(\frac{2x^3}{\lambda^3} - \frac{3x^2}{\lambda^2} + 1\right) + \dot{U}\left(\frac{6\dot{\lambda}x^2}{\lambda^3} - \frac{6\dot{\lambda}x^3}{\lambda^4}\right)\right]xdx = 2M_0 \tag{8}$$

or

$$m\left(\frac{3}{20}\ddot{U}\lambda^2 + \frac{3}{10}\dot{U}\dot{\lambda}\lambda\right) = 2M_0 \tag{9}$$

which can be written in the form of

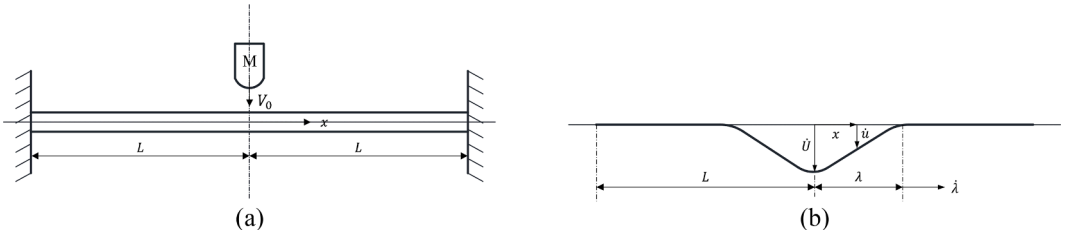

Fig. 9. (a) Impact of a fully clamped beam with a mass M and velocity V_0, (b) Transverse velocity field during the first phase of motion ($0 \le t \le t_1$).

$$\frac{d\left(\dot{U}\lambda^2\right)}{dt} = \frac{40M_0}{3m} \tag{10}$$

Integrating Eq. (10) with respect to time, and using the initial condition $\lambda = 0$ when $t = 0$, it gives the location-time characteristic of the travelling hinge as

$$t = \frac{3m\dot{U}\lambda^2}{40M_0} \tag{11}$$

and substituting Eq. (6) into (11), it yields

$$t = \frac{3mMV_0\lambda^2}{40M_0(M+m\lambda)} \tag{12}$$

Then, differentiating Eq. (12) with respect to time on both sides, it predicts the velocity of the travelling hinge as

$$\dot{\lambda} = \frac{20M_0(M+m\lambda)^2}{3mMV_0\lambda(2M+m\lambda)} \tag{13}$$

Fig. 10 graphically illustrates the change of effective length over time derived from Eq. (12) as well as the relationship between wave velocity and effective length derived from Eq. (13). As can be seen that the effective length increases in a varied velocity and the wave velocity is decreasing as the effective length increases.

It is evident from Fig. 7(a) that the transverse displacement at any position x in the beam is zero until the time $t(x)$ when the travelling hinge reaches x. Thus, the transverse displacement at a position x for a time $t \geq t(x)$ can be expressed as

$$u(t,x) = \int_{t(x)}^{t} \dot{u}(x)dt \tag{14}$$

where $\dot{u}$ is given by Eq. (2a), and the time $t(x)$ is predicted by Eq. (12) with $\lambda = x$. Since $\dot{\lambda} = d\lambda/dt$, replacing dt by $d\lambda/\dot{\lambda}$, Eq. (14) can be written as

$$u(t,x) = \int_{x}^{\lambda} \dot{u}(x)d\lambda/\dot{\lambda} \tag{15}$$

Now substituting Eq. (2a), (6) and (13) into Eq. (15), it gives

$$u(t,x) = \int_{x}^{\lambda} \frac{V_0}{\left(1+\frac{m\lambda}{M}\right)}\left(\frac{2x^3}{\lambda^3} - \frac{3x^2}{\lambda^2} + 1\right) \frac{3mMV_0\lambda(2M+m\lambda)}{20M_0(M+m\lambda)^2}d\lambda \tag{16}$$

which can be calculated numerically using Matlab [25]. Then, the deflection distribution along the beam can be obtained.

This phase of motion is completed when the travelling hinges reach the supports, i.e., $\lambda = L$, and according to Eq. (12), the corresponding time t_1 is

$$t_1 = \frac{3mMV_0L^2}{40M_0(M+mL)} \tag{17}$$

It should be pointed out that the above derivations assume the mid-span of the beam moves together with the drop weight with a velocity V_0 at the instant of impact, where the acceleration process is ignored. The predicted beam mid-span deflection $U(t)$ using Eq. (16) thus could be larger than the real case. To obtain a more accurate deflection during this phase of motion, $U(t)$ could be modified using the contact force between the drop weight and the beam.

With the contact force $P(t)$, vertical force equilibrium for the central portion of the beam between the two travelling hinges $0 \leq x \leq \lambda$ demands that

$$2\int_{0}^{\lambda} m\ddot{u}(x)dx = P(t) \tag{18}$$

Since the shear force Q is zero at the travelling hinges, substituting Eq. (2a) into (18) it gives

$$2\int_{0}^{\lambda} m\left[\ddot{U}\left(\frac{2x^3}{\lambda^3} - \frac{3x^2}{\lambda^2} + 1\right) + \dot{U}\left(\frac{6\dot{\lambda}x^2}{\lambda^3} - \frac{6\dot{\lambda}x^3}{\lambda^4}\right)\right]dx = P(t) \tag{19}$$

or

$$m\ddot{U}(t)\lambda(t) + m\dot{U}(t)\dot{\lambda}(t) = P(t) \tag{20}$$

where the location of the travelling hinge $\lambda(t)$ and its velocity $\dot{\lambda}(t)$ can be obtained using Eq. (12) and (13). Therefore, the modified mid-span deflection $U'(t)$ during the first phase of motion can be obtained by solving Eq. (20) numerically. And the modified deflections at other locations of the beam can be obtained by multiplying the ratio of $\frac{U'(t)}{U(t)}$ as

$$u'(t,x) = u(t,x)\frac{U'(t)}{U(t)} \tag{21}$$

and the deflected shape can be calculated by

$$\phi_1(t,x) = \frac{u(t,x)}{U(t)} \tag{22}$$

Since each time instant t corresponds to a specific mid-span deflection U, the shape function can also be written as a function of U similar to $\phi_1(U,x)$. The impact forces can be predicted using the empirical formula proposed by Li et al. [22]. The above calculated beam deflection, velocity, and acceleration at the end of the first phase will be passed to the second phase of motion as the initial conditions.

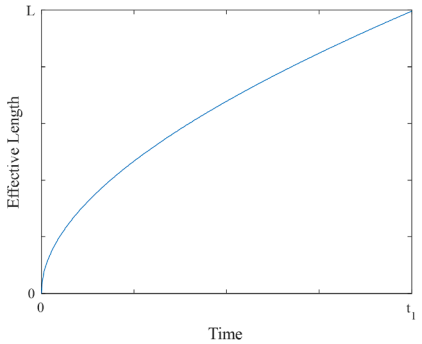

(a) Effective length vs. time

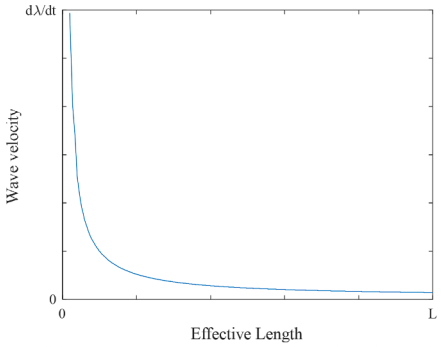

(b) Wave velocity vs. effective length

Fig. 10. Illustration of the relationships between (a) effective length and time; and (b) wave velocity and effective length derived from Eqs. (12) and (13).

3.2. Global response phase (Second phase of motion)

In the second phase of motion, the entire beam is excited. To predict the beam response during this phase, SDOF analysis method can be employed. However, as the test results above shown in Section 2.2.3, the mass factor is constantly changing with deflection and time in the global response phase, because the deformation shape of the beam changes over time leading to a time-dependent deformation shape function. Thus, a time-dependent mass factor should be considered for more accurate prediction of beam response. An improved SDOF analysis method is proposed in this study which considers time-dependent shape function and mass factor in the derivation of the SDOF system.

3.2.1. Time-dependent shape function and mass factor

In derivation of the SDOF system, the deflection shape of the beam is a key parameter to characterize the behavior of the structure. In the conventional SDOF models, two different deformation shapes are commonly assumed, i.e., elastic and plastic deformation shapes, respectively. Since wave propagation effect is not conventionally considered, in classical SDOF analysis, the initial conditions of the beam, i.e., initial deflection, velocity and acceleration, are all zero:

$$K_M^E M_b \ddot{U}(t) + R(U) = P(t) \tag{23}$$

$$K_M^P M_b \ddot{U}(t) + R(U) = P(t) \tag{24}$$

where K_M^E is the mass factor in elastic range and K_M^P is the mass factor in plastic range ($K_M^E = 0.37$ and $K_M^P = 0.33$ based on Biggs [26]).

To provide more accurate predictions of the dynamic response, the time-dependent deformation shape and mass factor are considered. Following the principle of SDOF analysis, the mid-span deflection is used to express the varying equivalent mass factor. To demonstrate the mass-factor-deflection characteristics, a simplified two-step mass-factor-deflection curve can be defined, as shown in Fig. 12.

Elasto-plastic stage: segment *AB*, when $U_1 < U < U_2$

Point A corresponds to the end of wave propagation phase when the flexural wave reaches to the supports, the corresponding midspan deflection U_1 is predicted by Eq. (20), and the deflection shape function at this instant is expressed as $\phi_1(U, x)$, thus, the mass factor K_1^M can be calculated by

$$K_1^M = \frac{2\int_0^L m\phi_1^2(U_1, x)dx}{M_b} \tag{25}$$

Since K_1^M is the mass factor at the end of the wave propagation phase, its value would be highly dependent on the impact velocity and impactor mass, as well as other factors that influence the wave propagation.

Point B refers to the starting point of total plastic response stage in the beam. Prior to Point B, the beam's behavior is dominated by elastic deformation. The deflection U_2 is set as the deflection corresponding to the peak resistance of the beam without the membrane effects. It is found that the obtained averaged peak mass factor (around 0.39) in the test is slightly higher than the mass factor of a fixed beam under static concentrated load (0.37). This is because the supports would yield during the impact process making the deformation shape more like an intermediate state between a fixed and a simply supported beam. Therefore, To estimate K_2^M, it is assumed that the average transverse velocity profile between Point A and Point B follows the average shape function of a fixed beam and a simply supported beam under concentrated load, $(\phi_{fix} + \phi_{sim})/2$, as shown in Fig. 11. Therefore, the deformation shape function at $U = U_2$ can be expressed as

$$\phi_2(x, U_2) = \frac{\left[U_1\phi_1(x, U_1) + \Delta U\left(\phi_{fix} + \phi_{sim}\right)/2\right]}{U_2} \tag{26}$$

where$\Delta U = U_2 - U_1$, ϕ_{fix} and ϕ_{sim} are the static shape functions of fixed beams and simply-supported beams under concentrated load respectively, in which

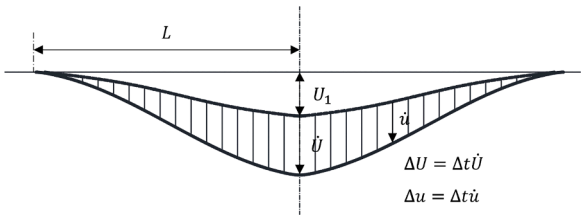

Fig. 11. Transverse velocity field during the second phase of motion.

$$\phi_{fix} = \frac{2x^3}{\lambda^3} - \frac{3x^2}{\lambda^2} + 1 \tag{27}$$

and

$$\phi_{sim} = \frac{x^3}{2L^3} - \frac{3x^2}{2L^2} + 1 \tag{28}$$

As a result, K_2^M can be calculated by

$$K_2^M = \frac{2\int_0^L m\phi_2^2(x, U_2)dx}{M_b} \tag{29}$$

Based on the laboratory test observation in Fig. 8, the mass-factor after wave reaching the supports is increasing almost linearly before reaching the maximum. Therefore, segment AB is simplified into a straight-line *AB* as shown in Fig. 12.

Plastic stage: segment *BC*, when $U > U_2$

In this stage, longitudinal reinforcements yield at the highest bending moment sections along the beam. Plastic deformation begins to accumulate quickly and dominate the response of the beam. The transverse velocity profile after Point *B* shifts to the static plastic shape which is linearly distributed. The plastic velocity profile can be expressed as

$$\dot{u}(x) = \dot{U}\left(1 - \frac{x}{L}\right),\ 0 \le x \le L \tag{30}$$

The deformation shape function in this stage is

$$\phi_3(x, U) = \frac{U_2\phi_2(x, U_2) + (U - U_2)\left(1 - \frac{x}{L}\right)}{U} \tag{31}$$

And the mass factor at $U > U_2$ is calculated as

$$K_M = \frac{2\int_0^L m\phi_3^2(x, U)dx}{M_b} \tag{32}$$

As a result, a time-dependent equivalent mass factor can be obtained

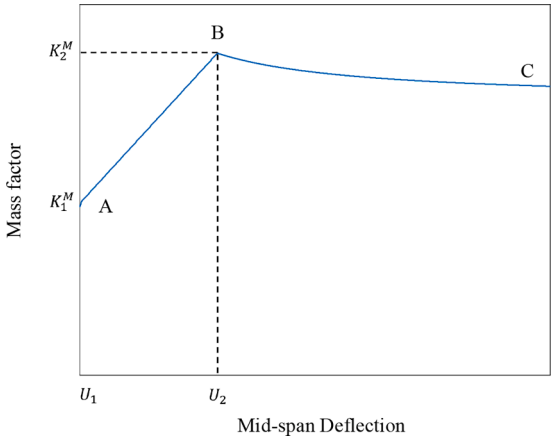

Fig. 12. Theoretical mass factor versus mid-span deflection curve.

through analytical solution, which takes into account the time-dependent deformation shape of the beam during global response phase when subjected to impact loading.

3.2.2. SDOF analysis

With consideration of the wave propagation effect and time-dependent deformation shape, the derived SDOF model can be used to predict its response during the global response phase. More explicitly, two methods are provided herein, i.e., Method I with known impact force time history, and Method II with known impactor mass and velocity.

3.2.2.1. Method I: SDOF system with known impact force time history. Classic SDOF analysis following Biggs' approach [26] can be performed with initial conditions obtained using Eq. (20) considering wave propagation effect, and time-dependent deformation shape functions. The dynamic response in the second phase can be expressed as

$$(K_M)_i M_b \left(\ddot{U}\right)_i + (R)_i = (P)_i \tag{33}$$

where $(K_M)_i$, $(R)_i$ and $(P)_i$ are the mass factor, resistance and the impact force at time *i*, respectively.

3.2.2.2. Method II: SDOF system (SDOF2) with known impactor weight and impact velocity. It is more common and likely that the detailed impact force time history is not known but only the impactor weight and impact velocity. In quantifying the response of the beam during the wave propagation phase, Eq. (16) can be employed, which assumes the impactor moves together with the beam at the instant of impact. For the global response phase, the equivalent mass of the SDOF system should consider both the weights of the beam and the impactor.

The equation of motion for the SDOF system can be expressed as

$$\left[(K_M)_i M_b + M\right]\left(\ddot{U}\right)_i + (R)_i = 0 \tag{34}$$

The initial conditions can be obtained through Eq. (16). This equation is valid to the condition that the drop weight remains on the beam and moves together with the beam. In reality, drop weight might rebound or does not move with the beam when they are at the same velocity and acceleration, if such conditions happened, the above equation would lead to incorrect predictions.

3.3. Summary of the proposed method

Fig. 13 summarizes the analysis procedures of the proposed methods for predicting the impact response of RC beams. The entire impact response is divided into two phases: local response (wave propagation) phase and global response phase. Upon obtaining pertinent information regarding the reinforced concrete (RC) element, it is possible to initially establish the resistance function R of the element in a theoretical manner. In the meantime, the impact force P can be estimated utilizing the existing impact force profile models. Subsequently, for the local response phase the effective length of the beam and wave propagation velocity can be computed using Eqs. (12) and (13). The deflections along the beam in the local response phase can be calculated using Eqs. (16) and (20). The end states achieved from the first phase serve as initial conditions for the subsequent global responses analysed via SDOF methods.

In method I, the knowledge of detailed impact force time history on the beam is known, the response of the beam during the global response phase can be calculated using the improved SDOF system – SDOF1, which is formulated by approximating the behaviour of a fully-fixed beam subjected to a concentrated impact load. The initial conditions for this system are derived from Eq. (20). Conventional SDOF analysis can then be performed to compute the response of the beam during the global response phase.

In contrast, if the impact force is unknown but only the impactor weight and impact velocity are known, Method II as illustrated in Fig. 13 can be employed. The derived equivalent SDOF system, denoted as SDOF2, considers the impactor and the beam as a single, unified element. The initial conditions are obtained from Eq. (16). Then, conventional numerical approach can be followed to calculate the beam response. Notably, the deflection calculated by Eq. (16) in the wave

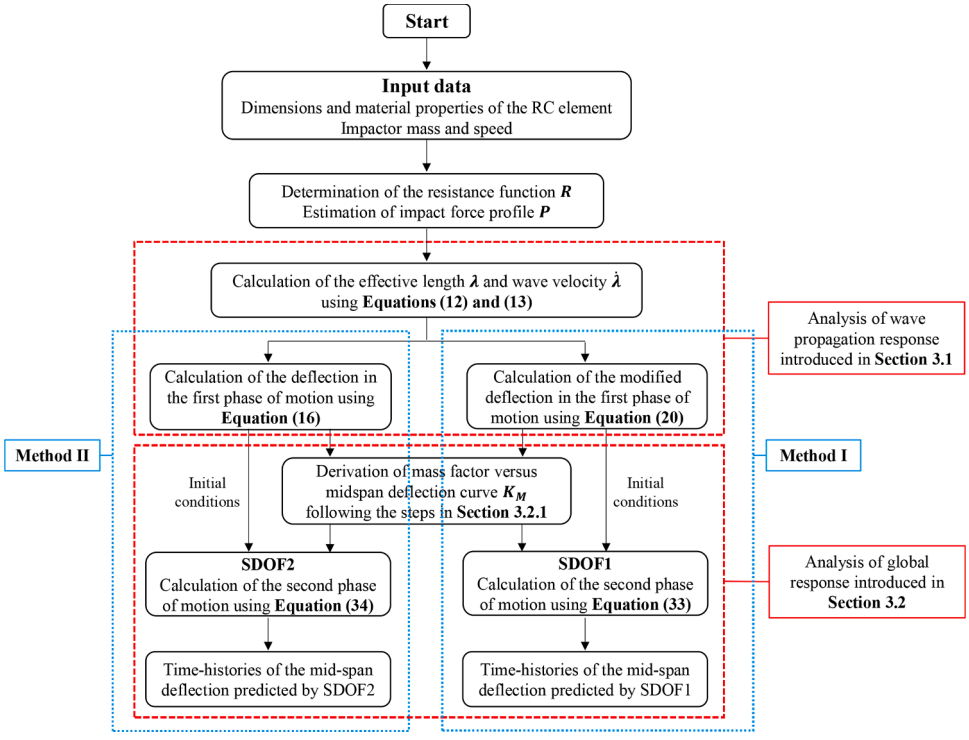

Fig. 13. Flowchart of the proposed analytical methods for predicting impact responses.

propagation phase could overpredict the real deflection of the beam because it overlooks the acceleration process of the structure. Method II mainly focuses on the maximum deflection that the structure could achieve, it could serve as a complementary approach to Method I, with their mutual verification acting as a mechanism to confirm the accuracy of the maximum deflection.

3.4. Prediction of beam impact response obtained in this study

The above proposed analysis methods are validated in this section to examine their suitability and accuracy in predicting the dynamic response of RC structural components under impulsive loading. It is firstly used to predict the beam responses as in Section 2. The prediction results are compared with the laboratory testing data to examine its accuracy. Derivation of the resistance function, wave propagation response, time-dependent mass factor, and the global response of the beams using the proposed methods are presented in detail to illustrate the proposed analysis method. To further validate the proposed methods, it is also used to predict and compare with impact testing results obtained by other researchers.

3.4.1. Derivation of resistance function

The resistance function of RC beams is firstly determined, where both compressive and tensile membrane actions are considered for fully-clamped beams. Previous studies proved that membrane actions could substantially increase the ultimate flexural load carrying capacity [19], which are thus important for obtaining more reliable predictions of structural dynamic responses. Fig. 14 shows a typical resistance function for restrained RC members considering membrane effects.

In the calculations of resistance functions, the membrane-force and midspan deflection relationship is firstly determined based on geometrical relationship of the deformed beam as shown in Fig. 15. The compressive membrane force-deflection relationship can be expressed as

$$\frac{dN}{df}=\frac{h(\eta_A+\eta_B)\frac{1}{0.5L}-u\frac{1}{0.5L}}{\frac{1}{S_n}+\frac{0.5L}{bhE_c+E_s(A_s+A_{ss})}} \tag{35}$$

where N represents the compressive membrane force induced by the lateral movement of the supports; f is the mid-span deflection of the beam; S_n is the lateral stiffness of support, which will be always compared with the elements' axial stiffness S_a that can be calculated by $S_s = 2bhE_a/L$, $E_a = [E_c(h-2\rho h_0)+2E_s\rho h_0)]/h$ [27]; ρ is the reinforcement ratio; E_c and E_s are the elastic modulus of concrete and reinforcement; x_n^A and x_n^B are the depths of the neutral axis (depth of compressive zone) of cross section A and B; A_s and A_{ss} are the area of reinforcement in tension and compression; L, h, b are the length, depth and width of the beam; I_a is the averaged moment of inertia of the beam

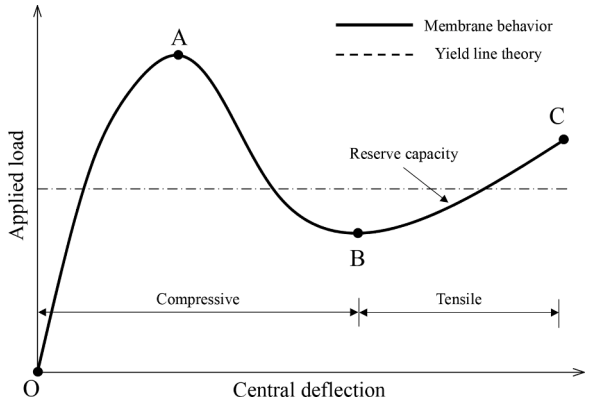

Fig. 14. Typical load-deflection relationship for restrained RC beams considering membrane effects [19].

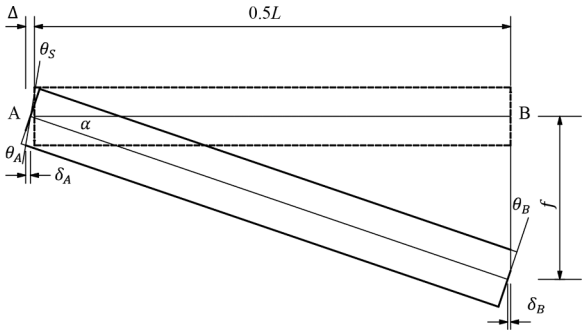

Fig. 15. Geometrical relationship of the deformed beam. [19].

which can be calculated following UFC 3–340–2 [16].

Incorporating the obtained membrane force into the layered analysis of cross-section [19], the moment-curvature relationship can be obtained. The midspan deflection of the RC beam can be calculated by integrating the curvature distribution over one-half the length of the RC beam. Finally, the load-midspan deflection relationship considering membrane actions can be derived.

For the above tested specimens DM1T1 and DM2T1 in Section 2, which are fully restrained, membrane actions are significant, while specimen DC1T1 is only restrained in rotational and vertical directions and no significant membrane actions are expected. Based on the observations [20], the lateral stiffness of specimens DM1T1 and DM2T1 could adopt the same stiffness as the axial stiffness of beam S_a. For DC1T1, although there are no lateral restraints, the rotational and vertical movements of the footing would cause substantial frictions between the footing and the floor, resulting in additional lateral restraints. The lateral stiffness of DC1T1 is about $0.05S_a$ [20]. It should be noted that strain rate effects are also accounted in calculating the resistance by multiplying the material strengths with different Dynamic Increase Factors (DIF). Following UFC 3–340–02 [16], the DIFs for concrete and steel are 1.25 and 1.23, respectively corresponding to a strain rate of $0.3s^{-1}$.

Fig. 16 shows the derived theoretical resistance-midspan deflection relationships of specimens DM1T1 and DC1T1. Given their identical design in terms of lateral restraining stiffness, specimens DM1T1 and DM2T1 have the same resistance. Conversely, specimen DC1T1, designed with a lower lateral restraining stiffness presents a diminished resistance. The maximum resistance of DM1T1 and DC1T1 are 99.1 kN and 70.2 kN, respectively. UFC approach predicts the ultimate resistance of a beam with a length of 2 L by

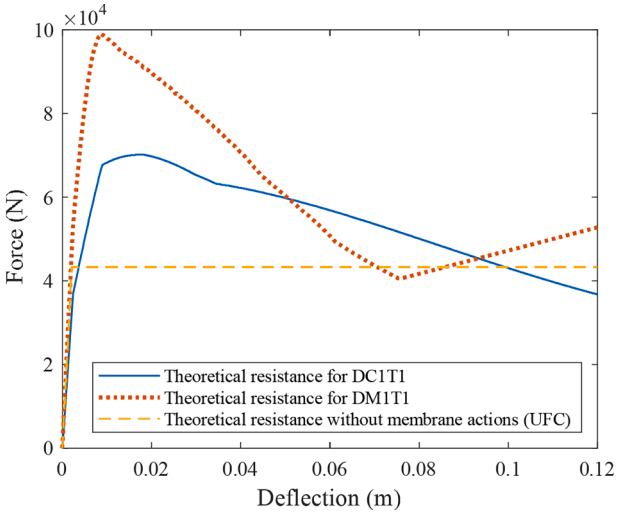

Fig. 16. Theoretical equivalent resistance for DM1T1 and DC1T1.

$$R_u = \frac{4M_u}{L} \tag{36}$$

where M_u is the ultimate moment capacity of the beam cross section which is computed by

$$M_u = A_s f_y d \tag{37}$$

in which d is the distance between the centroids of the compression and the tension reinforcement. Since membrane effect is not considered, UFC 3–340–02 [16] suggests the same resistance function for all those specimens. As can be seen, the resistance provided by the design standard is an elastic-perfectly-plastic model with the ultimate resistance of 43.3 kN, which is much smaller than those that consider membrane actions.

3.4.2. Wave propagation response

Substituting the structural data and impactor information into Eqs. (12) and (13) yields the effective length of the beam and wave propagation velocity at various moments. Since the parameters for all specimens are identical, their effective length and wave velocity variations are thus identical, as illustrated in Fig. 17. It takes 2.01 ms for the stress wave to propagate from mid-span of the beam to reach the supports. With the increase in beam effective length, wave velocity initially drops quickly, and the reduction rate then slows down gradually. The calculated velocity of the wave is 283 m/s when it reaches support.

Fig. 18 displays the predicted beam deflection profiles (a half beam) at time t_1 when the wave reaches the supports. The yellow dashed curve represents the deflection profile of DC1T1 and DM1T1 obtained via Eq. (16), which has a midspan deflection, $U(t_1)$, of 13.3 mm. The blue solid and red dashed-dot curves represent the modified deflection profiles for specimens DC1T1 and DM1T1, with almost identical mid-span deflections, $\dot{U}(t_1)$, of 2.6 mm and 2.8 mm, respectively. The difference is mainly because of some small variations in impact forces. These two profiles are generated by normalizing the yellow dashed curve with the ratio $\frac{\dot{U}(t_1)}{U(t_1)}$, where $\dot{U}(t_1)$ is derived from Eq. (20). The impact forces used in Eq. (20) are illustrated in Fig. 4a.

3.4.3. Derivation of time-dependent mass factor

The time-dependent mass factor to be used in the SDOF analysis can be derived following Section 3.2.1. Fig. 19 presents the theoretically derived mass factor obtained through the proposed analysis method incorporating time-dependent deformation shapes, where the mass factors derived from the experimental results in Section 2 are also included for comparison. Conventional mass factors suggested by UFC that are commonly used in analysis and design are also included. As can be seen, after the wave propagation phase, the beam has an equivalent mass factor of 0.22 and a midspan deflection of 2.6 mm for beam

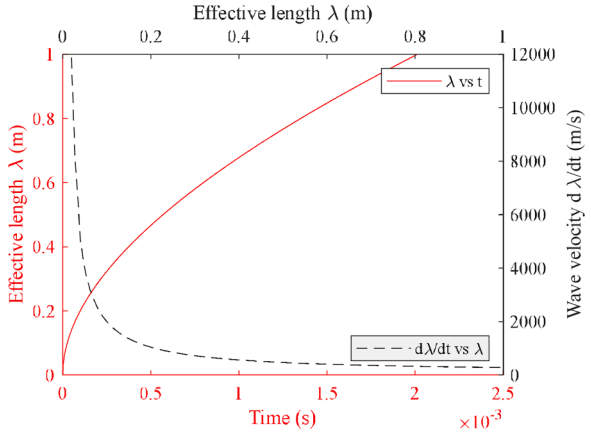

Fig. 17. Effective length γ and wave velocity at different time of the beam.

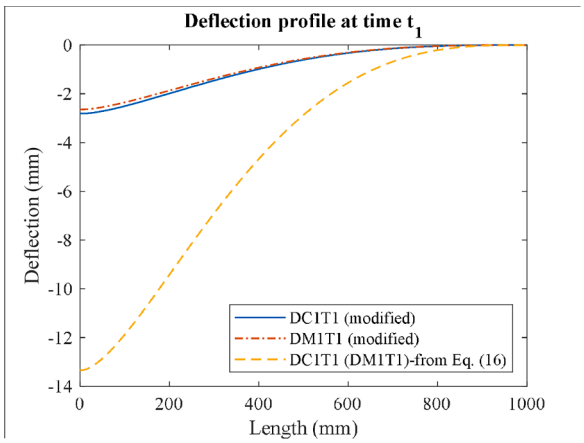

Fig. 18. Deflection profile of the beam at the end of wave propagation phase.

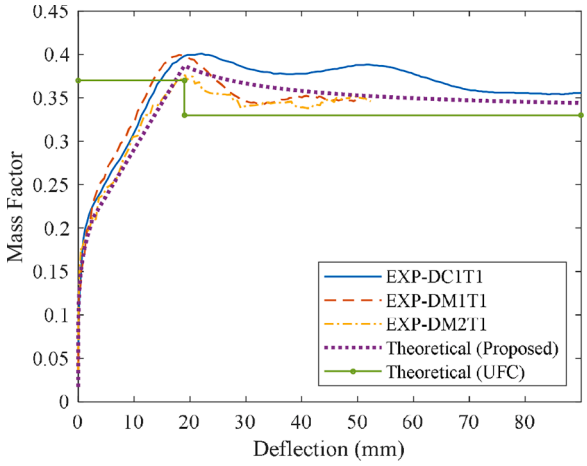

Fig. 19. Comparison between the theoretically derived mass factor and the test results.

DM1T1. The mass factor then experiences a linear increment until the midspan deflection attains a value of 19.0 mm, corresponding to a peak mass factor of 0.39. Subsequently, the mass factor exhibits a gradual decline, approaching the value of 0.33 gradually. It is obvious that the proposed model could reliably depict the actual trend of change in the mass factor. In contrast, the UFC-recommended mass factor is a constant value of 0.37 for the elastic phase before beam yielding and 0.33 thereafter for the plastic response, which significantly differs from the test results. This comparison demonstrates the significance of properly considering the wave propagation effect and time-dependent shape function.

3.4.4. Prediction of global responses

SDOF analysis is performed to predict the global responses of the RC beams, as explained in Section 3.2.2. Fig. 20 compares the midspan deflection time histories from the laboratory testing data and the analytical results. The recorded impact forces of DM1T1 and DC1T1, as illustrated in Fig. 4, are used to compute the responses. The results denoted as Proposed SDOF1 and Proposed SDOF2 are obtained following the two approaches shown in Fig. 13. While the Conventional SDOF results are calculated through Eqs. (23) and (24), which employ the constant mass factors but the same resistance functions as those in the Proposed SDOF1 and SDOF2. As can be seen, the proposed analytical methods demonstrate a high degree of accuracy in predicting beam responses when compared to the conventional method. However, some noticeable discrepancies can be observed between the time-deflection

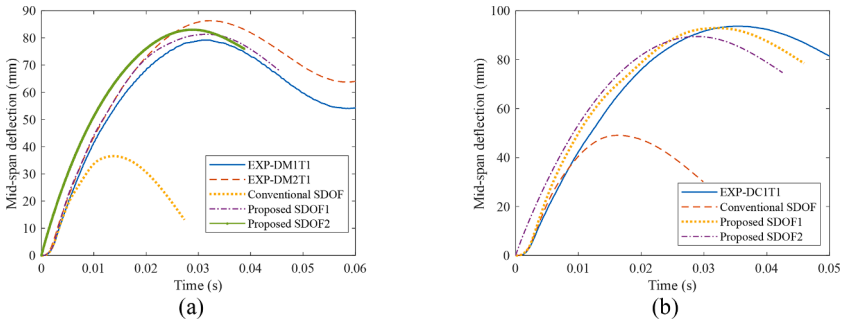

Fig. 20. Analytical and test results of impact responses for specimens (a) DM1T1 (DM2T1) and (b) DC1T1.

curves generated by SDOF1 and SDOF2, as the results from SDOF2 consistently exceed those calculated by SDOF1 before attaining the maximum deflection. This distinction can be attributed to the initial conditions in Method II, where the midspan of the beam is presumed to move at the same velocity as the impactor from the outset, while in Method I the beam starts to move with zero initial conditions. As the input energy remains consistent and energy loss due to impactor-beam interaction is minimal, the ultimate deflections are expected to be similar. Conversely, the predictions derived from the conventional SDOF analysis significantly underestimate the beam response, primarily because this approach neglects wave propagation effects and variations in mass factors. As in the early stage of the motion, only a small portion of the beam mass is mobilized, and the equivalent mass factor remains smaller initially even during the global response phase. While the traditional SDOF systems apply a much larger mass factor throughout the early stage of motion, which results in lower acceleration and velocity, leading to a significantly reduced final deflection.

Table 3 summarizes the maximum midspan deflection and the corresponding time required to attain the peak deflection. A close examination reveals that the proposed analytical methods demonstrate a significantly higher degree of accuracy in predicting the maximum midspan deflections of the beam, with the majority of errors falling within a 10% margin. Conversely, the results generated by the conventional SDOF method exhibit an average error exceeding 50%. This comparison underscores the efficacy of the proposed modified SDOF models in characterizing the impact response behavior of the specimens with a greater precision than the conventional SDOF method.

The above comparison proves the suitability and accuracy of the proposed improved analysis method over conventional SDOF approach. However, it should be noted that Method I (referred to as SDOF1 in the figures) is contingent upon the knowledge of impact force throughout the entire calculation process, and its accuracy is heavily reliant on the reliability of the impact force prediction. In contrast, Method II (denoted as SDOF2 in the figures) assumes continuous contact between the impactor and the beam before the beam reaches the maximum deflection, thus neglecting the interactions between them. Consequently, its results primarily depend on the characteristics of the beams and interaction scenarios between beam and impactor. In general, these two methods could be used to verify each other to ensure the rationality of the predictions. Further investigations would be carried out to study the suitability of these two methods in different scenarios, e.g., when the impactor and the beam have different mass ratios, or when the beam has different span-to-depth ratios.

3.5. Further validation

To further validate the suitability and accuracy of the proposed analysis approach, study by Fujikake et al. [8] on the impact response of RC beams is employed for further comparison with the predictions generated by the proposed methods. Fig. 21 shows the specimen details and the impact test setup. The beam S1616 was simply supported over a span of 1.4 m and had an effective mass of 126 kg. A 400 kg drop hammer was released to impact freely onto the top surface of the beam at midspan from a height of 1.2 m.

Fig. 22(a) presents the impact force recorded in the laboratory test, while Fig. 22(b) displays the theoretical resistance function of specimen S1616 derived in this paper. Based on the structural characteristics, the effective length and wave velocity over time are calculated and presented in Fig. 23. As shown, the wave velocity is noticeably higher than that of the beams tested in this study, with respective velocities of 1060 m/s and 283 m/s when the waves reach the supports. As derived from Eq. (17), a smaller impact velocity and a larger sectional moment capacity lead to the higher wave propagation velocity. Additionally, this beam spans only 1.4 m, resulting in a much shorter wave propagation time of merely 0.35 ms to reach the supports. The deflection profiles at the end of wave propagation phase are displayed in Fig. 24. Using Eq. (16), the mid-span deflection at the end of the wave propagation phase is 1.51 mm, while the estimated mid-span deflection is just 0.02 mm by using the modified profile. Apparently, during the wave propagation phase, both the duration and mid-span deflection are extremely small.

Nevertheless, the derived dynamic deformation shape differs from the static deformation shape. Following the proposed method in Section 3.2 above, the mass factor at the beginning of global response is predicted as 0.366 which differs substantially from that suggested by UFC 3–340–02 (K_m=0.49). In the global response phase, because of consideration of time-dependent beam deformation shape function, the

Table 3
Summary of the maximum deflections and the corresponding time from analytical methods and laboratory tests.

Specimen	Maximum mid-span deflection (mm)				Time reaching the maximum deflection (ms)			
	Test	SDOF0*	SDOF1	SDOF2	Test	SDOF0*	SDOF1	SDOF2
DM1T1	79.2	36.5 (−53.9%)	81.3 (2.7%)	83.0 (4.8%)	31.9	13.8 (−56.7%)	31.8 (−0.3%)	29.1 (−8.8%)
DM2T1	86.3	36.5 (−57.7%)	81.3 (5.8%)	83.0 (−3.8%)	32.4	13.8 (−57.4%)	31.8 (−1.9%)	29.1 (−10.2%)
DC1T1	93.7	49.1 (−47.6%)	92.9 (−0.9%)	89.5 (−4.5%)	35.6	16.2 (−54.5%)	32.2 (−9.6%)	29.0 (−18.5%)
S1616	36.8	22.0 (−40.2%)	38.1 (3.5%)	37.0 (0.5%)	17.8	10.1 (−43.2%)	16.9 (−5.1%)	17.4 (−2.2%)

* SDOF0 means the conventional SDOF method.

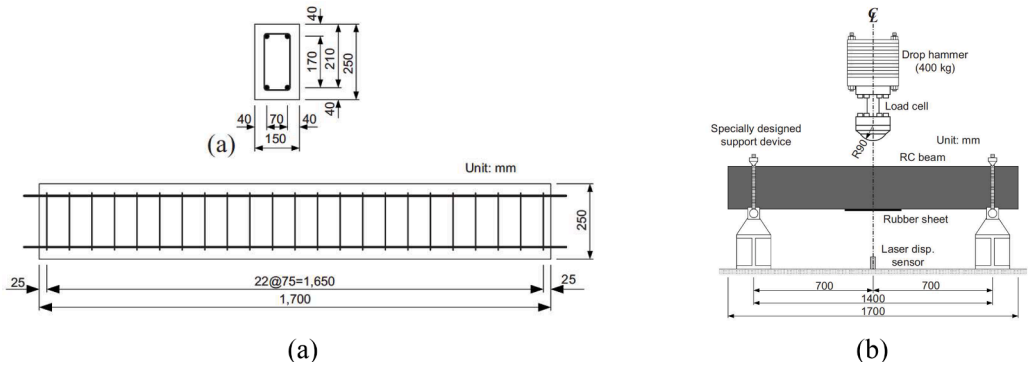

Fig. 21. (a) Specimen details and (b) drop hammer impact test setup [8].

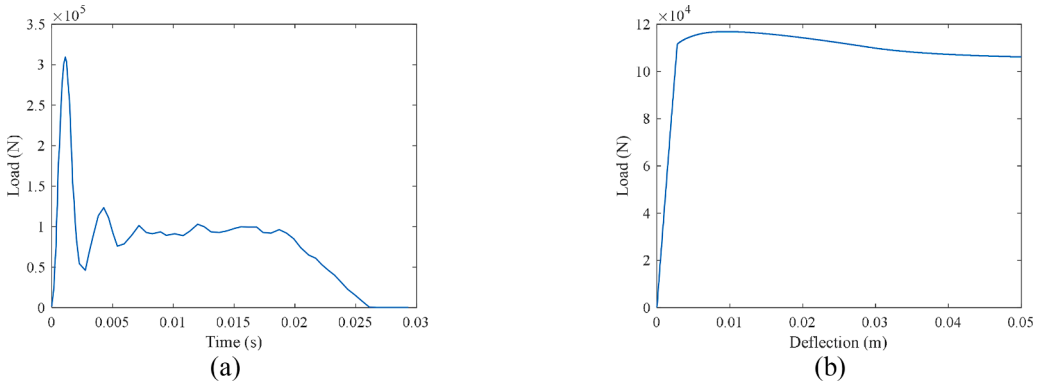

Fig. 22. (a) Impact force of specimen S1616; (b) Theoretical resistance function of specimen S1616.

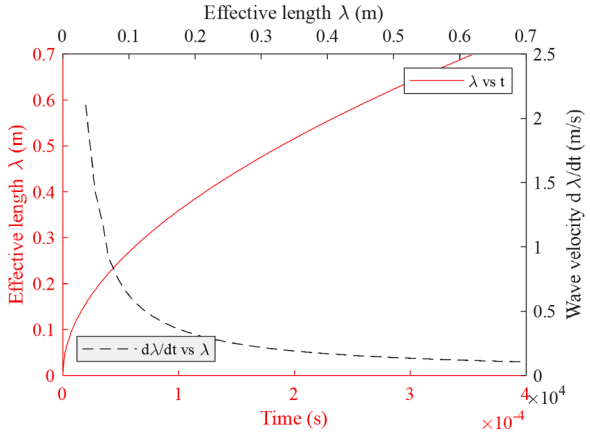

Fig. 23. Effective length γ and wave velocity at different time of Fujikake's beam.

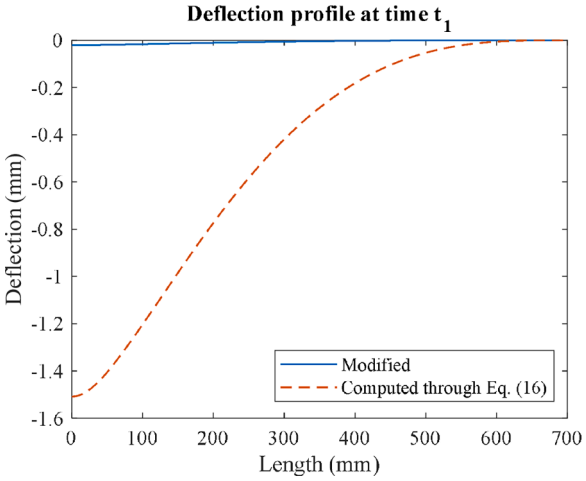

Fig. 24. Deflection profile of Fujikake's beam at the end of wave propagation phase.

equivalent mass factor increases from 0.366 linearly to 0.49 in the elastic range, after which it gradually decreases towards 0.33 in the plastic range. In contrast, the UFC standard recommends employing a constant mass factor of 0.49 in the elastic range and a constant mass factor of 0.33 in the plastic range (as compared in Fig. 25). The beam's global response is subsequently predicted through the SDOF method. Fig. 26 compares the midspan deflection time histories of the beam predicted by the proposed approaches in this study and that from the laboratory test. The analytical results from the proposed SDOF methods align well with the test results, while the response predicted by the conventional SDOF method is much smaller. The conventional SDOF method yields an error over 40%, while the errors from the modified methods are within 6%. This is because the conventional SDOF model adopts a larger mass factor from the onset of response, leading to smaller accelerations.

The above comparison demonstrates again that the proposed analytical approaches, which take into consideration both the wave propagation effects and time dependent deformation shape, could give more accurate predictions of impact response compared to the conventional SDOF method.

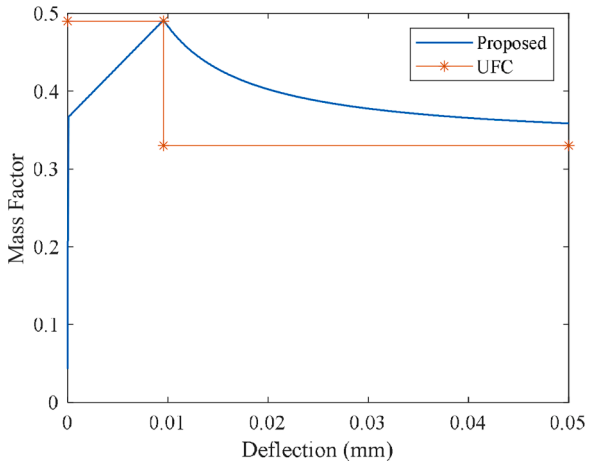

Fig. 25. Theoretical mass factor of specimen S1616 under impact.

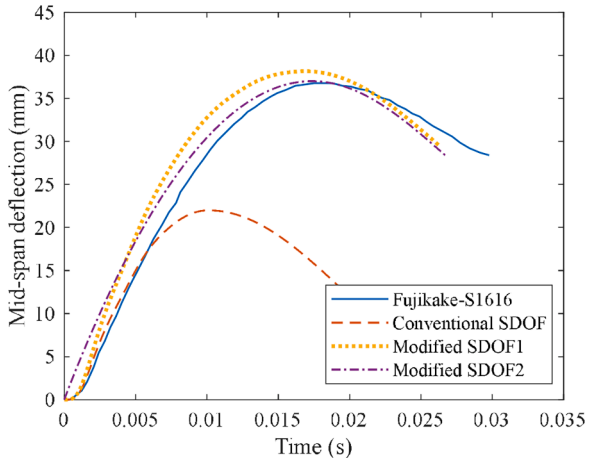

Fig. 26. Comparison of impact responses between analytical and test results.

4. Conclusion

This paper introduced improved analytical methods to predict the dynamic response of reinforced concrete (RC) beams with consideration of wave propagation effect and time-dependent shape function for Single Degree of Freedom (SDOF) analysis. The response of a structural component is divided into two phases: local response phase, which is calculated using governing equations; and global response phase analyzed using the improved SDOF methods. Two analytical methods are developed, where Method I can predict structural response if the impact load time history is available, while Method II only requires impactor weight and impact velocity.

Laboratory impact tests were designed and performed on three RC beams, whose dynamic responses were carefully monitored using a high-speed camera. The proposed analytical methods were then used to predict the dynamic responses of the tested beams. Comparison demonstrates that the proposed analysis methods could provide accurate predictions of the impact response of the tested beams, with most errors within 10%. In contrast, the conventional SDOF method exhibited significantly larger errors, averaging over 50%. The findings of this study confirmed that the proposed analytical approaches offer a more accurate and reliable estimation of the impact response of RC beams compared to the conventional SDOF method. Additional model validation is also performed against impact testing data reported by other researchers, which further verified the suitability and accuracy of the proposed method.

It is worth nothing the limitations of SDOF analysis method in predicting dynamic responses: Since all structures possess many degrees of freedom, the dynamic response of a structures may not be always adequately described by a single vibration mode, particularly for the cases with complex geometry and loading conditions. Furthermore, existing SDOF method exhibits difficulties in capturing the real internal force or stress characteristics across different cross-sections of the structure. Addressing these limitations in future research could greatly aid in evaluating the potential failure patterns of structures subjected to impulsive loading.

CRediT authorship contribution statement

Liuliang Cui: Conceptualization, Methodology, Investigation, Software, Writing – original draft. **Xihong Zhang:** Conceptualization, Methodology, Writing – review & editing, Supervision, Funding acquisition. **Hong Hao:** Conceptualization, Methodology, Writing – review & editing, Supervision, Funding acquisition.

Declaration of Competing Interest

The authors declare the following financial interests/personal relationships which may be considered as potential competing interests: Xihong Zhang reports financial support was provided by Australian Research Council.

Data availability

Data will be made available on request.

Acknowledgement

The authors would like to acknowledge the financial support from Australian Research Council under Discovery Project fund DP190103253.

References

[1] Bischoff PH, Perry SH. Compressive behaviour of concrete at high strain rates. Mater Struct 1991;24:425–50.
[2] Malvar LJ. Review of static and dynamic properties of steel reinforcing bars. Mater J 1998;95:609–16.
[3] Fujikake K, Senga T, Ueda N, Ohno T, Katagiri M. Study on impact response of reactive powder concrete beam and its analytical model. J Adv Concr Technol 2006;4:99–108.
[4] Cotsovos DM, Stathopoulos ND, Zeris CA. Behavior of RC beams subjected to high rates of concentrated loading. J Struct Eng 2008;134:1839–51.
[5] Zhang XX, Abd Elazim AM, Ruiz G, Yu RC. Fracture behaviour of steel fibre-reinforced concrete at a wide range of loading rates. Int J Impact Eng 2014;71:89–96.
[6] Isaac P, Darby A, Ibell T, Evernden M. Experimental investigation into the force propagation velocity due to hard impacts on reinforced concrete members. Int J Impact Eng 2017;100:131–8.
[7] Pham TM, Chen W, Hao H. Review on impact response of reinforced concrete beams: contemporary understanding and unsolved problems. Adv Struct Eng 2021;24:2282–303.
[8] Fujikake K, Li B, Soeun S. Impact response of reinforced concrete beam and its analytical evaluation. J Struct Eng 2009;135:938–50.
[9] Yi W-J, Zhao D-B, Kunnath SK. Simplified approach for assessing shear resistance of reinforced concrete beams under impact loads. ACI Struct J 2016:113.
[10] Jones N. Structural impact. Cambridge university press; 2011.
[11] Pham TM, Hao H. Effect of the plastic hinge and boundary conditions on the impact behavior of reinforced concrete beams. Int J Impact Eng 2017;102:74–85.
[12] Graff KF. Wave motion in elastic solids. Courier Corporation; 2012.
[13] Saatci S, Vecchio FJ. Effects of shear mechanisms on impact behavior of reinforced concrete beams. ACI Struct J 2009.
[14] Ožbolt J, Sharma A. Numerical simulation of reinforced concrete beams with different shear reinforcements under dynamic impact loads. Int J Impact Eng 2011;38:940–50.
[15] Jiang H, Chorzepa MG. An effective numerical simulation methodology to predict the impact response of pre-stressed concrete members. Eng Fail Anal 2015;55:63–78.

[16] UFC3-340-02, structures to resist the effects of accidental explosions, Washington DC, unified facilities criteria. 2008.
[17] Anderson TA. An investigation of SDOF models for large mass impact on sandwich composites. Comp Part B 2005;36:135–42.
[18] Cui L, Zhang X, Hao H. Improved analysis method for structural members subjected to blast loads considering strain hardening and softening effects. Adv Struct Eng 2021. 13694332211007382%@ 13694332211001369-13694332211004332.
[19] Cui L, Zhang X, Hao H, Kong Q. Improved resistance functions for RC elements accounting for compressive and tensile membrane actions. Eng Struct 2022;251:113549.
[20] Cui L, Zhang X, Hao H. Experimental investigation of resistance function of RC beam considering membrane effects. Eng Struct 2022;267:114602.
[21] Zhao D-B, Yi W-J, Kunnath SK. Numerical simulation and shear resistance of reinforced concrete beams under impact. Eng Struct 2018;166:387–401.
[22] Li H, Chen W, Pham TM, Hao H. Analytical and numerical studies on impact force profile of RC beam under drop weight impact. Int J Impact Eng 2021;147:103743.
[23] AS3600-2018, concrete structures. Sydney: Standards Australia Limited; 2018.
[24] Li H, Chen W, Hao H. Factors influencing impact force profile and measurement accuracy in drop weight impact tests. Int J Impact Eng 2020;145:103688.
[25] Moler CB. Numerical computing with Matlab. SIAM; 2004.
[26] Biggs JM. Introduction to structural dynamics. New York: McGraw-Hill Book Company; 1964.
[27] Chen L, Fang Q, Guo Z, Liu J. An improved analytical method for restrained RC structures subjected to static and dynamic loads. Int J Struct Stab Dyn 2014;14:1350052.